Available online at www.sciencedirect.com
ScienceDirect
Journal of the European Ceramic Society 30 (2010) 1267–1275
www.elsevier.com/locate/jeurceramsoc

Sanitary-ware vitreous body characterization method by optical microscopy, elemental maps, image processing and X-ray powder diffraction

A. Pagani[a], F. Francescon[b], A. Pavese[a,c], V. Diella[a,*]

[a] National Research Council, IDPA, Section of Milan, Via Botticelli 23, I -20133 Milan, Italy
[b] Ideal Standard International, C.O.E., Ceramic Process Technology, Via Cavassico Inferiore 160, I-32026 Trichiana, BL, Italy
[c] Dipartimento di Scienze della Terra, Università di Milano, Via Botticelli 23, I-20133 Milan, Italy

Received 26 June 2009; received in revised form 15 October 2009; accepted 6 November 2009
Available online 16 December 2009

Abstract

The present investigation deals with a characterization method for fired body (cast piece) from a standard sanitary-ware industrial cycle, relying upon data mainly from optical/electron microscopy and chemical mapping. Image processing techniques have been used to reconstruct the phase-distribution throughout the body, so as to provide a phase-arrangement-sensitive description of the crystalline and amorphous components. The results so attained are compared with those from classical X-ray powder diffraction in terms of total phase-contents. The amorphous phase-content and its distribution can be determined by optical microscopy, and the modest level of precision of the phase quantification is improvable by accounting for the occurrence of voids. Residual quartz is identified by means of the backscattered electron contrast differences in images, and thereby its morphologic properties and amount are determined. The use of elemental X-ray maps allows one to attain a description of the local composition and, on the basis of some assumptions, to quantify microcrystalline mullite and also discriminating between primary *versus* secondary mullite.

Keywords: Firing; X-ray methods; Optical microscopy; Spectroscopy; Traditional ceramics

1. Introduction

It is long known that the physical properties of the sanitary-ware bodies after firing are dependent on a variety of aspects: the constituent phases resulting from the high temperature reactions involving the minerals used,[1,2] the developed microstructures[3,4] and the degree of densification.[5–7] In particular, the complexity of the occurring transformations and of the starting mineralogical composition (kaolinite, clay-minerals, quartz and feldspar) makes it difficult to predict and govern the properties of the resulting vitreous ceramics.[8] In sanitary-ware the content of amorphous phase forming upon firing can amount to greater than 60 wt% and is a function of the original slip's mineralogical composition,[9,10] the filler particle size and the flux type, as well as of the basic processing variables, such as firing temperature and heating time.[7,11] The relevant sanitary-ware processing output complexity requires a characterization of the vitreous body to determine not only the phase-content,[12] but also to fix the spatial/compositional distribution of the phases involved,[13] with particular care to the amorphous one, providing thereby a basic link to the notion of microstructure and, as a consequence, to the macroscopic mechanical properties.

Although an effective characterization of the occurring phases[14] in a vitreous body is a difficult task because of their compositional and spatial inhomogeneity, a contribution to this purpose can be achieved by combining traditional techniques (X-ray powder diffraction and optical microscopy) with high spatial-resolution methods based on the use of electron microprobe (scanning electron microscopy, wavelength dispersive spectrometry) and image processing techniques.

In this view, the aim of the present work is to point out the development of such an approach, complementary to conventional X-ray powder diffraction,[15] that allows one to characterize a vitreous body on the basis of image/mapping-type data, intrinsically sensitive to and informative of the spatial distributions of the phases involved. In this way we mean to provide a description that is able to complement the traditional notions of "phase-occurrence" and "phase quantification" with those

---

[*] Corresponding author. Tel.: +39 02 503 15621; fax: +39 02 503 15597.
E-mail address: valeria.diella@idpa.cnr.it (V. Diella).

0955-2219/$ – see front matter © 2009 Elsevier Ltd. All rights reserved.
doi:10.1016/j.jeurceramsoc.2009.11.008

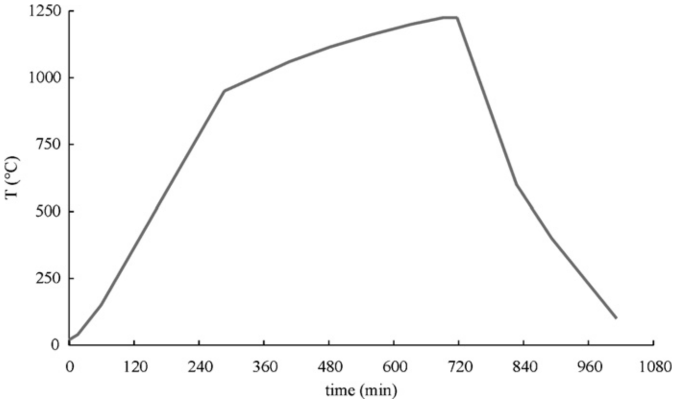

Fig. 1. Time–temperature profile of the heating firing cycle.

of “phase-arrangement” and “local phase-content” throughout a solid. For such a purpose, we have resorted to laboratory techniques ranging from X-ray powder diffraction, to scanning electron microscopy, optical microscopy and wavelength dispersive spectrometry on thin sections of the ceramic product. We focus on the sanitary-ware bodies from a pilot plant, and use samples which have undergone a time–temperature (*t–T*) profile representative of a common *t–T* cycle of the industrial firing process, so that this study will be as close as possible to the conditions of the usual practice of wholesale production and hence be ready for a transfer to an industrial platform.

2. Experimental

2.1. Sample

The analyzed samples are 11 mm unglazed rectangular (50 mm × 100 mm) tiles fired at a peak temperature of 1245 °C (Fig. 1) in a pilot industrial kiln; the starting slip was prepared from the following commercial raw materials: 25 wt% ball clay, 25 wt% kaolin, 22 wt% quartz and 28 wt% sodium feldspar. We report in Table 1a the raw materials’ phase-compositions, determined by X-ray powder diffraction, and in Table 1b their chemical compositions, as provided by the raw materials suppliers.

Ten uniformly spaced sections parallel to the smaller face of a sample tile were chosen, and the related thin sections carved, to provide a representation of the whole body. In order to reduce their number, the smallest set of thin sections required to yield steady results was sought, following Marinoni et al.[16] This led us to observe that five uniformly spaced thin sections are sufficient to provide a faithful representation of the body, and hereafter they are termed “reference thin sections” (RTSs).

The reproducibility of the results here reported has been confirmed on the basis of many repetitions of the full experimental procedure, which encompasses slip formation and casting, firing of the body, thin section carving, data collection and data-analysis. The oscillations of the *t–T* profile and of the slip-forming raw materials composition have been restrained within those commonly occurring in the industrial practice. Although the results discussed here refer to a specific batch, they are fully representative of the most general observations obtainable from the large-scale production.

2.2. X-ray powder diffraction (XRPD)

The X-ray powder diffraction patterns were collected by a PANalytical X’pert Pro diffractometer, equipped with an X’Celerator detector, using CuK$_\alpha$-radiation, a step size of 0.02° 2θ and a total collection time of 18 min. The General Structure Analysis System (GSAS) software[17] has been used for processing the XRPD patterns.

A parallelepiped was carved from each tile and ground to a ≈15–10 μm particle size powder to investigate the phase-components of the fired body. NBS-corundum was added to allow a quantification of the amorphous phase, following the approach reported by Gualtieri.[18,19] We use five independent

Table 1
(a) Mineralogical composition of the raw materials used for the initial slip; (b) chemical composition of the raw materials as given by the suppliers.

a

wt%	Raw material (industrial name)	Mineralogical composition (wt%)				
		Kaolinite	Illite	Quartz	Feldspar (albite)	Glass
25	Kaolin	84.5(2)	7.6(2)	3.0 (1)	4.9 (5)	–
25	Ball clay	34.5(2)	5.5(2)	5.6 (1)	0.5 (3)	53.9 (4)
22	Quartz	–	–	100	–	–
28	Feldspar	–	–	14.4 (1)	85.6 (2)	–

b

Raw material	Chemical composition (wt%)							
	SiO_2	Al_2O_3	Fe_2O_3	MgO	TiO_2	CaO	K_2O	Na_2O
Kaolin	54.25	41.82	1.08	0.34	0.06	0.08	2.26	0.17
Ball clay	55.65	39.52	1.38	0.23	1.04	0.23	1.73	0.23
Quartz	99.42	0.40	0.05	0	0	0.02	0.05	0.05
Feldspar	71.29	18.07	0.13	0.1	0.06	0.20	0.10	10.04

The term “glass” is used to encompass amorphous and highly defective/poorly crystalline phases.

samplings to fix a phase-composition representative of the fired body, as preliminary tests proved that increasing the number of samplings gives results no more than 1σ discrepant with respect to those obtained according to the adopted procedure.

2.3. Partitioning of RTSs into sub-areas and choice of the image scale

In order to provide a reliable description of the spatial distribution of any observable and measurable feature, or object, in the ceramic body, the images recorded by optical and/or electronic microscopy have been collected following a judiciously chosen sampling scheme. It requires every RTS to be partitioned into "sub-areas" (hereafter we use this term to address such cells): each one corresponds to one image and provides one value for any measured observable. The number of sub-areas ($n_{\text{s–a}}$) is a critical parameter of our processing, as it affects the determination of the distribution of an observable throughout the body and depends on the recording technique used.

$n_{\text{s–a}}$ has been fixed on the basis of a partitioning such that varying the number of sub-areas does not affect significantly the final results. In fact, we observed that: (i) for low $n_{\text{s–a}}$ values, a general coarsening of features (for instance, those defined by means of pixel grey scale intervals) occurs; (ii) for $n_{\text{s–a}}$ within a given range, features are neatly observable and invariant with respect to the partitioning (*i.e.* somewhat of a "restricted scale invariance"); (iii) for large $n_{\text{s–a}}$ values, incoherence grows, so that diffuse randomness and general featurelessness characterize the pattern. In this view, we fix the sub-areas number as a small but reliable value lying in the range of stability, corresponding to point (ii).

Pictures were taken using as large as possible a magnification, compatible with the features of interest and the instrumental resolution limits. Low magnification implies loss of the finest details, including those small crystal grains embedded in the glass matrix and having a size comparable to the image spatial resolution. On the other hand, high magnification gives an overestimation of the finest details at the expenses of those sensitive to a large scale, which are poorly represented in such a collection configuration.

2.4. Optical microscopy (OM)

A transmission optical microscope Leica MS5, interfaced to a 4.1 Gigapixel Nikon Coolpix 990 digital camera was used, equipped with a device that allows the rotation of the polarizer–analyzer system with respect to the lens system. In this way, it was possible to collect photographs in different extinction positions – two at least – without changing the orientation of the sample. Digital images, having a dimension of 2272 × 1704 pixels and a resolution of about 0.5 pixel/μm, were collected at a 100× magnification (Fig. 2), partitioning every half thin section into 18 sub-areas.

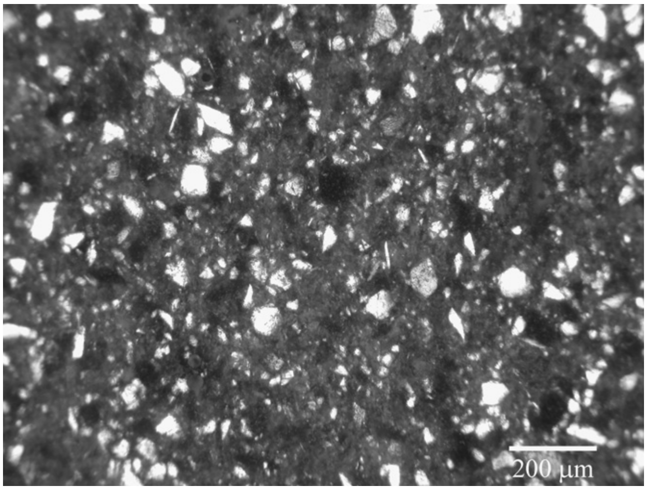

Fig. 2. OM digital image (crossed Nicols; 100×): the amorphous and microcrystalline matrix appears black/dark-grey.

In so doing, one can exploit the systematic extinction of the amorphous phase at normal polarizer–analyzer configuration (*i.e.* 90°), whereas non-cubic minerals, like quartz and mullite, have a high probability of occurring at a non-extinction position, save the improbable case of the alignment of a mineral's optic axis and that of the microscope. This allows one to record images at different polarizer-sample–analyzer orientations so that the crystal grains are likely to be, at least once, light (*i.e.* grey level in a 8 bit grey scale image; processing by Image-Pro Plus 4.5 software, Media Cybernetics Inc., 2001), whereas the amorphous matrix is always set at full extinction (*i.e.* dark in grey scale). The congruent pixels of an image taken at different sample orientations are then superposed in order to generate a binary mask whose black regions are attributed to glass; the dark regions can be separated from the light ones, due to crystal grains, by choosing an appropriate threshold for the grey scale.[16,20,21]

2.5. Scanning electron microscopy (SEM)

Backscattered electron (BSE) and secondary electron (SE) images on the reference thin sections were collected by means of a Tescan VEGA TS 5136XM SEM (accelerating voltage: 20 kV, magnification: 400×), partitioning a surface of about 250 mm^2 per RTS into 30 sub-areas. The images (1024 × 1024 pixels; resolution of 4.3 pixels/μm– Fig. 3) were processed and analyzed by the same code used for the OM-pictures.

2.6. Electron microprobe analyses (EMPA)

A JEOL JXA-8200 SuperProbe electron microprobe analyzer was used to collect elemental X-ray emission maps in wavelength dispersive spectrometry (WDS) for Al and Si (accelerating voltage: 15 kV, probe current: 5×10^{-9} A, magnification: 1000×; 769 × 769 digital pictures with a resolution of 7.7 pixels/μm), following the same sampling scheme used in the case of the BSE-images.

The Al content was preliminarily used to differentiate compositional areas, which were then investigated in detail to determine their full chemical- and mineralogical composition, and to fix the spatial phase-arrangement thereby. Note that the electron beam spot size on the sample covers an area of about 1 μm in diameter, and is shifted to scan the surface at nominally 1 μm per step. The excited sample volume expands into the bulk with a "pear-like" shape of ≈2–3 μm largest radius; this means that the elemental X-ray maps obtained provide coverage of the explored surface virtually without overlapping between adjoining areas, but with a possible degree of superposition between bulk volumes.

High-precision compositional data were collected from a number of sampled points throughout the body for the quantification of Si, Al, Ca, Na, K and Fe. The analyzing system was operated using an accelerating voltage of 15 kV, a beam current of 15 nA and a counting time of 30 s on peak and 10 s on background. A series of natural minerals (wollastonite for Ca and Si, anorthite for Al, K-feldspar for K, omphacite for Na and fayalite for Fe) were adopted as standards. The results were corrected for matrix effects by a conventional ZAF routine from the JEOL software package. The instrument sensitivity is estimated to be about 0.02 wt% of the analyzed element, on the basis of previous calibrations on reference compounds.

2.7. Homogeneity and spread indexes (HI and SI)

To concisely describe the nature of the distribution throughout a body of the values per sub-area of a given *o*-observable (*o*-value-distribution) measured by image analysis, we use an index[22] defined as follows:

$$\mathrm{HI} = 1 - \frac{\sigma}{\Delta} \tag{1}$$

where Δ is the difference between the upper and lower *o*-values, and σ corresponds to the *o*-variable statistical standard deviation. HI (homogeneity index) ideally tends to ~0.71 for a fully uniform distribution of the *o*-variable over a Δ – broad range, to ~0.83–0.88 in the case of a Gaussian-like distribution assuming the observed *o*-values to lie in an interval as large as 6–8σ, and to unity when just one value is allowed for *o* (full homogeneity).

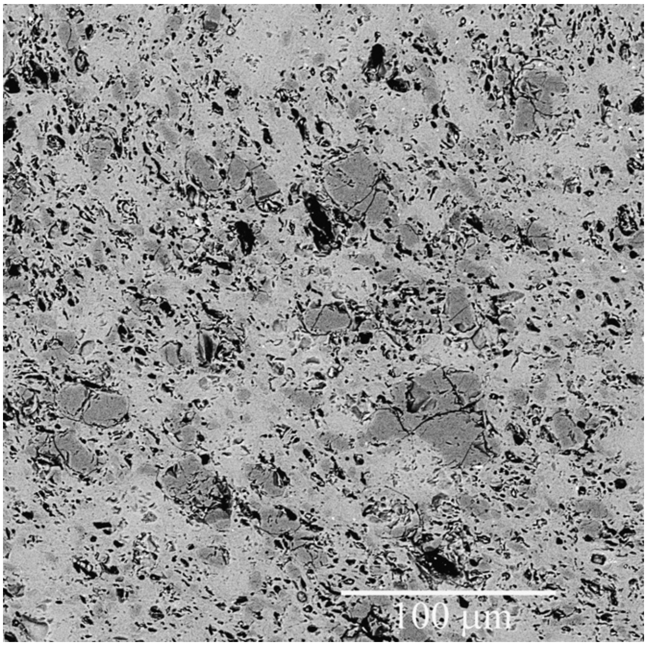

Fig. 3. An example of backscattered electron image (400×).

It is useful to introduce also a further auxiliary "spread index", defined as

$$\mathrm{SI} = \frac{\Delta}{\mu} \tag{2}$$

where μ stands for the average *o*-value. SI measures the "impact" the scattering of the *o*-values has on their average; a small SI suggests a "dense" gathering of the *o*-values within a comparatively narrow "band".

The degree of homogeneity of the spatial-arrangement of the *o*-variable can be assessed in terms of occurrence of an *o*-gradient, which is numerically calculated on the basis of the *o*-values associated to the sub-areas and along a given direction. Moreover, the *o*-gradients have been re-calculated by further fractioning each sub-area into two and three equally sized cells, to verify the stability of the results as a function of the partitioning. Note that a limitation of the method in its present fashion is that only intra-thin section gradients are measured, whereas those inter-thin sections are not.

2.8. Image processing

Let us assume to have a multiphase system, shaped as a parallelepiped $A \times h$, where A is a face and h its normal edge, for which a set of $\Phi(x,y,z)_j$ functions are defined, such that $\Phi(x,y,z)_j = 1$, if the (x,y,z)-point is occupied by the jth-phase, and $\Phi(x,y,z)_j = 0$ otherwise; let the total volume occupied by the jth-phase be V_j. It follows immediately that

$$V_j = \int_0^h \mathrm{d}z \int_A \Phi(x, y, z)_j \mathrm{d}x\mathrm{d}y \tag{3}$$

The integration above can be replaced by its numerical approximation, taking into account that

$$V_j \approx \sum_{k=1,N} \Delta z_k \int_A \Phi(x, y, z_k)_j \mathrm{d}x\mathrm{d}y \tag{4}$$

where N is the number of the z-axis normal sections used. If $\Delta z_k = \Delta z_j$, *i.e.* the sections are uniformly spaced, then Eq. (4) is re-cast into

$$V_j \approx \frac{h}{N} \sum_{k=1,N} \int_A \Phi(x, y, z_k)_j \mathrm{d}x\mathrm{d}y.$$

The $\Phi(x,y,z_k)_j$-function is built by digitalizing the corresponding $\mathrm{z_k}$-section's image and using the grey(hue)-scale to associate each pixel to a given phase. Therefore one attains

$$V_j \approx \frac{h}{N} \sum_{k=1,N} \sum_{m=1,M} \Phi(x_m, y_m, z_k)_j \Delta A$$

where ΔA is the surface fraction attributed to a pixel, namely A/M, if M is the number of pixels used to represent a section. Altogether, one has

$$V_j \approx \frac{(hA)}{N} \frac{\sum_{k=1,N} \sum_{m=1,M} \Phi(x_m, y_m, z_k)_j}{M} \tag{5a}$$

and the percentage contribution of V_j to the total volume is

$$V(\%)_j \approx \frac{1}{N}\frac{\sum_{k=1,N}\sum_{m=1,M}\Phi(x_m, y_m, z_k)_j}{M} \tag{5b}$$

Eq. (5b) allows one to readily calculate the weight percentages of the phases involved once their densities are known.

A more complex situation occurs if each pixel cannot be attributed to one phase only, but it results from a manifold contribution, such as our case of the elemental X-ray maps. These latter are provided as arrays whose terms bear the oxide contents measured on $\approx$1–2 μm^2 bathed areas, corresponding to active volumes of $\sim 10\pi$ μm^3. Therefore, one has to unfold the contributions of the different phases to every pixel for a correct estimation of the bulk phase-occupancies. Let ν_j be the weight percentage of the jth-phase related to a given pixel, then the relationship linking the occupied j-volume to ν_j is

$$V_j \propto \left(\frac{V_j^M}{M_j}\right)\nu_j \tag{6}$$

where V_j^M and M_j are molar volume and mass of the jth-phase. In this view, one definitively attains

$$p_j = \frac{W_j \nu_j}{\sum_{l=1,\text{phases}} W_l \nu_l} \tag{7}$$

where p_j is the fractional volume contribution of the jth-phase to a given pixel and $W_j = (V_j^M/M_j)$. Given that Eq. (7) must hold for any pixel, it is necessary for the sake of generality to introduce one index more, *i.e.* $p_{j,n}$, where n explicitly fixes the nth-pixel. Eventually, one sets the $\Phi(x_n,y_n,z_n)_j$ function of the jth-phase at the nth-pixel equal to $p_{j,n}$.

An estimation of the relative uncertainty affecting the quantities inferred from Φ can be attained by the ratio σ/μ. μ and σ refer to the average and expected standard deviation of the grey scale or hue scale, values of the pixels attributed to the same class, *i.e.* those assumed to represent the same feature (for instance, the same chemical composition or phase).[23]

3. Results and discussion

3.1. XRPD phase quantification

The mineralogical composition of the fired body was determined on the basis of five independent measurements for each sample, as stated above, to reliably appreciate oscillations, and results in 18.6(±1.3) wt% quartz, 19.8(±1.8) wt% mullite and 61.6(±2.7) wt% glass; bracketed are the expected standard deviations from the Rietveld analysis.

The refined cell parameters for mullite are shown in Table 2, along with those reported by Schneider et al.[24] and related to the mullite type. The observed *a*-parameter, that shows a significant sensitivity to composition, is fully consistent with a 3:2-mullite type. *b*, conversely, lies closer to that of a 2:1-mullite rather than a 3:2-mullite; however, both *b*(2:1-mullite) and *b*(3:2-mullite) reference values do not divert from ours more than 3σ and, in such a view, the *b*-edge cannot provide a robust discriminative marker. The *c*-edge does not allow one to reliably distinguish between the two types of mullite, whereas the measured *V* is consistent with a 3:2 composition. Altogether, (i) our lattice parameters agree with those of 3:2-mullite, *i.e.* $Al_{4+2x}Si_{2-2x}O_{10-x}$ with *x*, number of oxygen vacancies per unit cell, ideally equal to 0.25 (see Lee et al.[25] about the complexity of attributing a well defined composition to mullite from firing), and (ii) no evidence of 2:1-mullite is observed by XRPD.

Table 2
Cell parameters and volume of mullite observed in the sample on study compared with those (*) from Schneider et al.[24].

Mullite type	Lattice parameters			
	a (Å)	*b* (Å)	*c* (Å)	*V* (Å^3)
3:2*	7.553	7.686	2.8864	167.6
2:1*	7.588	7.688	2.8895	168.6
Present work	7.553 (3)	7.696 (3)	2.8853 (2)	167.7

3.2. Glass content and distribution: the role of optical microscopy

The image analysis of the OM digital pictures yields a 79.2(±0.4) vol% fraction of glass, corresponding to $\approx$76(±0.4) wt% (density of glass estimated about 2.34 g/cm^3 using the Fluegel model[26]; $\rho_{\text{quartz}} = 2.62$ g/cm^3, $\rho_{\text{mullite}} = 3.05$ g/cm^3), on the basis of the dark threshold fixed as the average over ten points sampled in a glass area. However, because of the resolution limit at 100× magnification, we have not been able to differentiate between the amorphous phase and micro-crystals embedded[27] therein. Furthermore, the voids are a hindrance to precision, as they are always extinct at normal “nicols” and leading therefore to an overestimation of the glass.

Although of modest precision, this technique can supply a qualitative evaluation of the spatial distribution of glass throughout the body, using the glass-fraction per sub-area as reference variable. In Fig. 4 we set out the glass concentration values per sub-area measured on a RTS, by way of example. The sample exhibits glass concentration values that densely gather within a narrow interval (SI = 0.07) imparting an HI equal to 0.73, *i.e.* bearing characteristics of a uniform but least-scattered value-distribution. This altogether suggests a remarkable homogeneity of the glass arrangement throughout the body, implying the absence of significant gradients outward or inward.

78.6	79.8	78.9	79.6	77.8	79.2
78.5	80.5	79.9	79.5	79.5	79.8
78.9	78.6	79.7	79.8	79.2	78.5

Fig. 4. Volume fraction distribution (%) of glass, determined by OM, in a half-section of a tile sample, using a grid of 18 sub-areas. The size of the scanned area is about 11 mm × 25 mm.

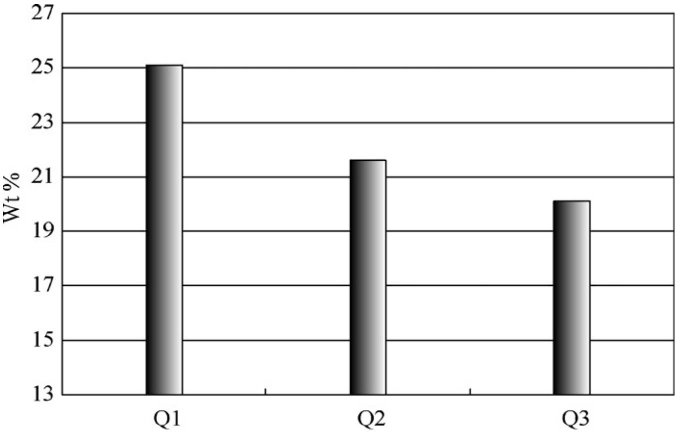

Fig. 5. Residual quartz after firing, as a function of quartz D_{50} (Q_1 = 59.6 μm, Q_2 = 24.0 μm, Q_3 = 9.8 μm). The results refer to fired bodies obtained using the same raw material composition and thermal cycle discussed in the text.

3.3. Quartz content and distribution: the role of scanning electron microscopy

BSE images have been collected by SEM and processed to determine the pore and residual-quartz fractions, their spatial-arrangements and concentration value-distributions (average electron density for quartz, 0.78, SiO_2-glass, 0.70 and mullite, 0.91 e/Å^3). The smallest detectable and morphologically distinguishable object has a linear size of about 0.5 μm. Macro-pores, which are readily fixed as not providing backscattered electrons, have been observed to generally correspond to "voids" of at least 1 μm diameter; they are intrinsic of the sample or due to the mechanic thin section making. Quartz was fixed by exploiting the BSE-contrast with respect to the embedding matrix, whereas this was not feasible for the small crystals of mullite (see next section), because of their size and because they are "immersed" into the surrounding silica-rich glass.

The particle size distribution of the quartz raw material, determined before firing by a conventional laser particle size analyzer, gives a residue of 9.4(±0.7) vol% below 2 μm, while the smallest grain size observed by microphotographs in the vitreous ceramic samples and attributable to quartz is from about 2 μm. This might mean that, on one hand, the resolving power of the backscattered electron contrast is insufficient to unambiguously discriminate so small objects and, on the other hand, a part of the 0.5–2 μm fine fraction of quartz has been consumed during heating, in keeping with Stathis et al.[7] The latter instance also agrees with a preliminary study we performed on the co-relation between starting-quartz average size and residual-quartz content after firing. Fig. 5 shows those results obtained using the same thermal cycle adopted. In the present investigation, a comparison between the quartz contents (determinations by XRPD) before and after firing yields about 28.1 and 18.6 wt%, respectively, in keeping with a loss of crystalline SiO_2 in favour of an amorphous component. Furthermore, Carty and Senapati[1] suggest the occurrence of amorphous silica from meta-kaolinite decomposition in melt formation at eutectic temperature (*i.e.* about 200 °C below the maximum firing temperature achieved) to hinder crystallization of quartz.

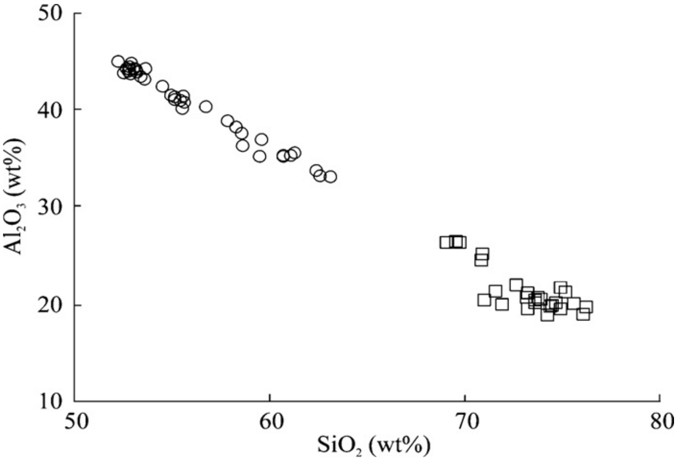

Fig. 6. Al_2O_3 *versus* SiO_2 content (wt%) in the matrix-zone of the fired body. Different symbols refer to the two main compositional ranges fixed to Al maps analysis: open circles stand for high-Al areas, referring to A-region, and open squares for low-Al areas, referring to B-region. One symbol corresponds to several measurements (see text).

Image analysis gives an average value for the quartz content of 16.8(±3.1) vol% [≈17.5(±3.2) wt%], providing mean HI and SI of 0.75 and 0.96, respectively. Macro-pores amount to 8.3(±1.4) vol% and are consistent with a distribution bearing mixed uniform and Gaussian characters (HI = 0.78 and SI = 0.80); no coherent pore-gradient through the tile volume occurs. Larger-than-1 μm-pore concentration is naturally overestimated because it is inclusive of voids intrinsic to the sample or due to the detachment of quartz grains during the preparation of the thin sections. Taking into account the contribution of voids, whether natural or induced, the estimation of the amorphous phase by OM changes from ≈79 to ≈71 vol%, *i.e.* about 67 wt%, which, though still providing an overestimation, yields a significantly more precise figure than the one obtained prior to the void-correction.

3.4. Al-bearing phases: the role of the elemental maps

Chemical maps have been used to characterize the glass component and track mullite throughout the samples. We first masked the portions of RTS's surface free of aluminium (*i.e.* quartz, amorphous silica, possible voids), and then focussed on the Al-bearing remaining area (Si–Al–glass and microcrystalline mullite[1,28–30]) forming the "matrix" which embeds the residual crystal grains. Fig. 6 shows the co-relation between alumina and silica contents over the matrix region, on the basis of about 60 randomly scattered analysis-points measured with as high as possible precision.

We have partitioned the matrix region as a function of an Al_2O_3-mapping, which provides Al-concentration values on a relative scale only, and then used the quantitative Al_2O_3–SiO_2 relationship (Fig. 6) to attribute an absolute composition to the pixels. We observe two Al_2O_3-content regions: (A) that in which alumina ranges from 45 to 33 wt% (average wt%: $SiO_2 \approx 57$, $Al_2O_3 \approx 39$, residual: K–Na–Fe–Mg–Ca-oxide); (B) that parted from the former by a large compositional gap and bearing

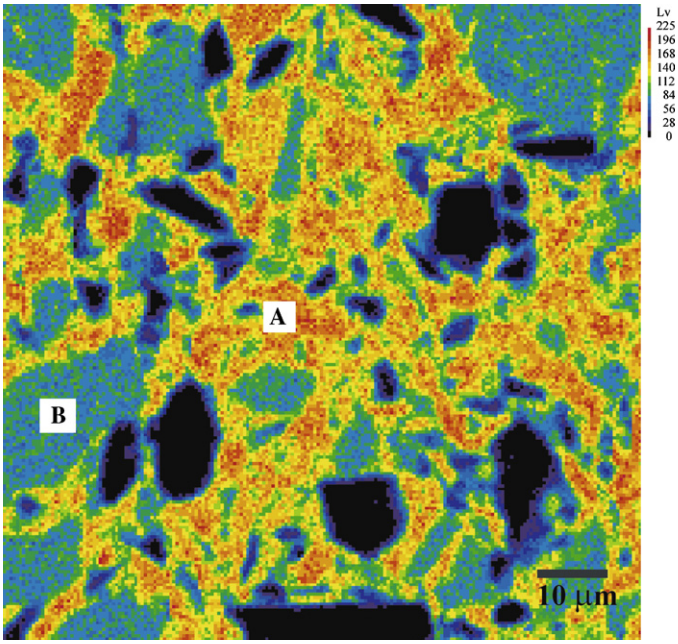

Fig. 7. EMP Al-map, wherein are visible Al-rich zones (A) and glassy matrix areas (B) bearing a feldspar-like composition. Dark regions are occupied by quartz grains and pores.

an Al_2O_3-content from about 25 to 20 wt% (average wt%: $SiO_2 \approx 73$, $Al_2O_3 \approx 20$, residual: Na–K–Fe–Ca–Mg-oxide). The Al_2O_3-rich(poor) A(B)-zone corresponds to areas of the Al-maps looking like the one marked by "A"("B") in Fig. 7. The average alumina(wt%)/silica(wt%) ratio of the A-region, ≈0.68, is consistent with areas that are related to residues of transformations involving aluminium-phyllosilicates, which bear alumina(wt%)/silica(wt%)≈0.84 (case of ideal kaolinite) and start undergoing de-hydroxylation above ≈400 °C.[28,30]

The A- and B-zones have also been analyzed in terms of their spatial distributions to assess the degree of homogeneity throughout the fired body, adopting a partitioning of each RTS into 30 sub-areas. This yields HIs as large as 0.70 and 0.75, and SIs of 0.62 and 0.83, for A and B, respectively. Such values provide an indication in favour of a tendency to uniform distributions of the A- and B-concentration values, especially for the former. Both A- and B-zones exhibit a prevalently homogeneous spatial-arrangement, free of any significant gradient. The A-zone/B-zone volume ratio, *i.e.* $V(A)/V(B)$, is estimated to be about 0.89.

We have separated the fully amorphous content of the matrix from crystalline phases by etching some RTSs (8 M fluoroboric acid for a 1 h long attack), so as to dissolve glass and preserve mullite/quartz crystals. XRPD quantitative analysis revealed the solid residue of etching to have the same mineralogical composition of the tile and the quasi-complete disappearance of glass, removed by the chemical attack. Analyzing SE-images, mullite crystals of three morphology classes have been observed (Fig. 8): (1) thick crystals of ≈0.1 μm linear size; (2) small needles, having length of about 1 or a few μm; (3) coarse elongated crystals, more than 10 μm in length. Crystals of type (1) are attributable to "primary mullite", in keeping with Lee and Iqbal[29] and Chen et al.[30]; those related to the second and the third cases exhibit almost the same aspect ratio *R* (defined as length/width), which ranges from slightly above 10 up to even beyond 30, and are consistent with "secondary mullite". The average *R* has been estimated to be ≈1 for primary mullite, and ≈15 for secondary mullite, on the basis of the observations on 40 randomly sampled mullite needle specimens recorded in SE-microphotographs of the acid etched thin sections.

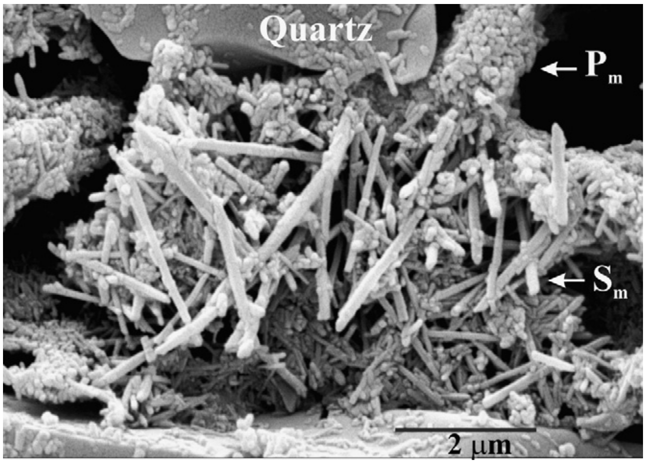

Fig. 8. Sample etched with BF_4H (BSE-image); mullite needles of different size and large aspect ratio. P_m and S_m indicate primary and secondary mullite, respectively.

The leached solution, analyzed by an induction-coupled plasma spectrometer in terms of Al and Si contents, reveals an Al_2O_3/SiO_2 weight ratio of 0.220(3) (determination over 10 samplings). On the basis of the results above, one can straightforwardly relate the fractions of alumina entering mullite in the A- and B-regions (λ_A and λ_B, respectively) to other measured quantities, using the mass conservation principle. One thus attains the relationship beneath:

$$\frac{[(1+\zeta)-(\zeta\Theta^{A}+\Theta^{B})/\Theta^{\mathrm{Glass}}]}{[1-1/(K_1K_2\Theta^{\mathrm{Glass}})]}=\zeta\lambda_{\mathrm{A}}+\lambda_{\mathrm{B}} \qquad (8)$$

where $K_1 = 1.5$ (*i.e.* alumina/silica ratio in 3:2-mullite), $K_2 = Al_2O_3/SiO_2$ molar weight ratio, $\Theta^J = SiO_2(\mathrm{wt\%})/Al_2O_3(\mathrm{wt\%})$ referred to the *J*th-region or in glass, $\zeta \approx [V(A)/V(B)] \times [Al_2O_3(\text{wt\% in A-region})/Al_2O_3(\text{wt\% in B-region})]$.

We now take for true that all alumina in the A-region enters primary mullite (*i.e.* $\lambda_A = 1$), in keeping with the hypothesis of a prevalent kaolinite-like origin of Al_2O_3 therein, whereas the remaining SiO_2 from the decomposed phyllosilicates participates in the amorphous silica-phase; this leads *via* Eq. (8) to $\lambda_B = 0.12$. The correctness of the assumption above can just be assessed *a-posteriori* by comparing the results attained with XRPD's.

Using the formalism introduced in Section 2.8, we estimate the content of mullite to be about 21.7(±3.8) wt%, whereas glass amounts to 60.8(±7) wt%, this latter determined as the complement to 100% of the concentrations of quartz (see the previous section) and mullite. Taking into account the agreement between the results from imaging with XRPD's [18.6(±1.3), 19.8(±1.8) and 61.6(±2.7) wt% for quartz, mullite and glass, respectively;

mean discrepancy, in terms of phase-composition, of ≈5.5%], one gathers that the assumption made above, *i.e.* $\lambda_A = 1$, provides a basically acceptable approximation. Should one try other partitioning schemes of the alumina fraction destined to form mullite in the A-region, $\lambda_A = 0.9$ for instance, one would attain a mullite content of 22.8 wt%, whose increasing deviation from the XRPD mullite-determination supports the validity of our choice, *i.e.* $\lambda_A = 1$.

Mullite of the A- and B-regions is calculated to be about 17.9 and 3.9 wt%, respectively, and yields a primary/secondary mullite ratio of about 4.6:1. In such a view, the $V(A)/V(B)$ ratio and the primary-secondary mullite contents are expected to be parameters significantly relatable to the technological response of a fired body, as they are associated to the efficacy of developing needle-interlocking microstructures[31–33] (see De Noni et al.[34] about the effect of the quartz particle size on the mechanical behaviour of porcelains).

4. Conclusions

The use of conventional and high-resolution optical techniques, along with electron probe micro-analyzer in combination with image processing methods, allows us to provide a detailed description of vitreous body from standard sanitary-ware production, in terms of phase-compositions and their related distribution throughout the sample. In particular, we list beneath the main conclusions achieved:

1. classical optical observations provide an approximated characterization of the glass distribution and concentration in the sample, exploiting the permanent extinction of the isotropic phases. The glass fraction value-distribution throughout the body exhibits the character of a uniform, least-scattered distribution (HI = 0.73, SI = 0.07), with a high spatial homogeneity; the total glass content is ≈10%-overestimated (≈67 wt%) with respect to the XRPD determination (≈61 wt%);
2. backscattered electrons have been used to determine the distributions and concentrations of quartz and of 0.5–1 μm larger macro-pores. Note that the latter are inclusive of the voids intrinsic to the sample or due to dislodging of grains during the thin section making. Both show concentration value distributions throughout the sample with uniform, or uniform-Gaussian, characters (HI = 0.75 and SI = 0.96, for quartz; HI = 0.78 and SI = 0.80, for macro-pores), and the total quartz content is determined (≈17 wt%) in agreement with the estimation by XRPD (≈18 wt%);
3. elemental maps and imaging have brought information about the matrix embedding quartz grains in the fired bodies. In particular: (i) the matrix can be partitioned into two compositional fractions, as a function of the alumina content (45–33 wt% and 25–20 wt%); (ii) the first region (A) corresponds to sample's zones bearing primary mullite, along with amorphous silica, while the second one (B) is related to secondary mullite and Al-Si-glass phases, mainly from feldspar decomposition; (iii) mullite exhibits three dominant morphologies: (iii.1) one bearing thick mullite crystals with an aspect ratio of ≈1; (iii. 2) a second one characterized by short needles, no longer than a few μm; (iii. 3) a third one having crystals of at least 10 μm (aspect ratio values of iii. 2–3 range from 10 to 30, with average about 15); (iv) the A- and B-concentration value-distributions show characters of uniform distributions and a tendency to average spatial homogeneity. The $V(A)/V(B)$ ratio is about 0.89, and leads to primary and secondary mullite contents of about 17.9 and 3.9 wt%, respectively, assuming $\lambda_A = 1$, *i.e.* all alumina in the A-zone contributes to form mullite.

In short, we conclude that the characterization method developed provides results consistent with those from XRPD (average discrepancy of about 5.5%), but enriched by details about the spatial-arrangement of the phases involved and the local composition of the vitreous ceramics. Such an aspect plays a relevant role to yield an effective and physically sound description of the phases composing a solid that exhibits a high degree of phase-inhomogeneity, like the sanitary-ware vitreous bodies (see Hyett et al.[35] about an investigation relying upon a spatially sensitive approach, based on XRPD area mapping).

Acknowledgement

The authors are indebted to Kevin Young (Sibelco, RDI Europe) for reading the text before submission and providing useful comments and remarks that improved the quality of the manuscript.

References

1. Carty WM, Senapati U. Porcelain – raw materials, processing, phase evolution and mechanical behaviour. *J Am Ceram Soc* 1998;**81**:3–20.
2. Sedmale G, Sperberga I, Sedmalis U, Valancius Z. Formation of high-temperature crystalline phases in ceramic from illite clay and dolomite. *J Eur Ceram Soc* 2006;**26**:3351–5.
3. Barbieri L, Bonfatti L, Ferrari AM, Leonelli C, Manfredini T, Settembre D. Relationship between microstructure and mechanical properties in fully vitrified stoneware. In: Vincenzini P, editor. *Ceramics: charting the future*, vol. 3A. Modena, IT: Techna SrL; 1995. p. 99–105.
4. Lee WM, Rainforth WM. *Ceramic microstructures*. UK: Chapman & Hall; 1995.
5. Hamano K, Wu YH, Nakagawa Z, Hasegawa M. Effect of grain size of quartz on mechanical strength of porcelain bodies. *J Ceram Soc Jpn* 1991;**99**:153–7.
6. Leonelli C, Bondioli F, Veronesi P, Romagnolo M, Manfredini T, Pellicani GC, et al. Enhancing the mechanical properties of porcelain stoneware tiles: a microstructural approach. *J Eur Ceram Soc* 2001;**21**:785–93.
7. Stathis G, Ekonomakou A, Stournaras CJ, Ftikos C. Effect of firing conditions, filler grain size and quartz content on bending strength and physical properties of sanitaryware porcelain. *J Eur Ceram Soc* 2004;**24**:2357–66.
8. Lee SM, Kim SK, Yoo JW, Kim HT. Crystallization behaviour and mechanical properties of porcelain bodies containing zinc oxide additions. *J Eur Ceram Soc* 2005;**25**:1829–34.
9. Sanchez E, Ortis MJ, Garcia J, de Lamus R. Effect of porcelain tile raw materials compositions on the arising phases in firing. *Ceram Acta* 1998;**9**:205–7.
10. Gislimberti A, Maschio RD, Campolo MP, Primio S. Porcelain stoneware. Correlation between chemical–physical properties of the raw materials and technological characteristics of the final product: durability and mechanical strength. *Ceram Acta* 1998;**9**:46–7.

11. Martin-Marquez J, De la Torre AG, Aranda MAG, Rincon JM, Romero M. Evolution with temperature of crystalline and amorphous phases in porcelain stoneware. *J Am Ceram Soc* 2009;**92**:229–34.
12. Chaudhuri SP, Sarkar P. Constitution of porcelain before and after heat-treatment I: mineralogical composition. *J Eur Ceram Soc* 1995;**15**:1031–5.
13. Dondi M, Ercolani G, Melandri C, Mingazzini C, Marsigli M. The chemical composition of porcelain stoneware tiles and its influence on microstructural and mechanical properties. *Interceram* 1999;**48**:75–83.
14. De la Torre AG, Bruque S, Aranda MAG. Rietveld quantitative amorphous content analysis. *J Appl Crystallogr* 2001;**34**:196–202.
15. Rietveld HM. A profile refinement method for nuclear and magnetic structures. *J Appl Crystallogr* 1969;**2**:65–71.
16. Marinoni N, Pavese A, Foi M, Trombino L. Characterisation of mortar morphology in thin sections by digital image processing. *Cement Concr Res* 2005;**35**:1613–9.
17. Larson AC, von Dreele RB. General structure analysis system (GSAS). Los Alamos National Laboratory Report LAUR 86-748, 2000.
18. Gualtieri AF. Modal analysis of pyroclastic rocks by combined Rietveld and RIR methods. *Powder Diffr* 1996;**11**:97–106.
19. Gualtieri AF. Accuracy of XRPD QPA using the combined Rietveld-RIR method. *J Appl Crystallogr* 2000;**33**:267–78.
20. Starkey J, Samantaray AK. A microcomputer-based system for quantitative petrographic analysis. *Comput Geosci* 1994;**20**:1285–96.
21. Fueten F. A computer-controlled rotating polarizer stage for the petrographic microscope. *Comput Geosci* 1997;**23**:394–416.
22. Martin BR. *Statistics for physicists*. London and New York: Academic Press; 1971.
23. Weeks AR. *Fundamentals of electronic image processing*. New York: IEEE Press; 1998.
24. Schneider H, Schreuer J, Hildmann B. Structure and properties of mullite—a review. *J Eur Ceram Soc* 2008;**28**:329–44.
25. Lee WE, Souza GP, McConville CJ, Tarvornpanich T, Iqbal Y. Mullite formation in clays and clay-derived vitreous ceramics. *J Eur Soc Ceram* 2008;**28**:465–71.
26. Fluegel A. Global model for calculating room-temperature glass density from the composition. *J Am Ceram Soc* 2008;**90**:2622–5.
27. Meani L. Tecniche convenzionali e non per la caratterizzazione dei prodotti post cottura dell'industria dei sanitari (conventional and unconventional techniques for the caracterization of post-firing products of sanitary ware industry). Geological Sciences Thesis, University of Milan; 2008.
28. Lee SM, Kim YJ, Moon H. Phase transformation sequence from kaolinite to mullite investigated by an EFTEM. *J Am Ceram Soc* 1999;**82**:2841–8.
29. Lee WE, Iqbal Y. Influence of mixing on mullite formation in porcelain. *J Eur Ceram Soc* 2001;**21**:2583–6.
30. Chen CY, Lan GS, Tuan WH. Microstructural evolution of mullite during the sintering of kaolin powder compacts. *Ceram Int* 2000;**26**:715–20.
31. Selsing J. Internal stress in ceramic. *J Am Ceram Soc* 1961;**44**:419–25.
32. Mattyasovsky-Zsolnay L. Mechanical strength of porcelain. *J Am Ceram Soc* 1957;**40**:299–306.
33. Palatzky A, Werner T. Increase the mechanical strength of porcelain bodies. *Silikat Technol* 1958;**9**:68–73.
34. De Noni Junior A, Hotza D, Soler VC, Vilches ES. Effect of quartz particle size on the mechanical behaviour of porcelain tile subjected to different cooling rates. *J Eur Ceram Soc* 2009;**29**:1039–46.
35. Hyett G, Green M, Parkin IP. X-ray diffraction area mapping of preferred orientation and phase change in TiO_2 thin films deposited by chemical vapour deposition. *J Am Chem Soc* 2006;**128**:12147–55.